Coupled Spin Ordering in the Ln_2LiRuO_6 Double Perovskites

Sophia J. Makowski,[†,‡] Jennifer A. Rodgers,[†] Paul F. Henry,[§] J. Paul Attfield,[†] and Jan-Willem G. Bos*[,†]

School of Chemistry and Centre for Science at Extreme Conditions, University of Edinburgh, West Mains Road, Edinburgh EH9 3JJ, United Kingdom, Department of Chemistry and Biochemistry, Ludwig-Maximilians-University, Butenandtstrasse 5-13, 81377 Munich, Germany, and Institut Laue-Langevin, BP 156, 38042 Grenoble Cedex 9, France

Received July 30, 2008. Revised Manuscript Received November 21, 2008

Synchrotron X-ray, neutron powder diffraction, and magnetic susceptibility measurements have been used to characterize the Ln_2LiRuO_6 (Ln = Pr, Nd, Sm, Eu, Gd, and Tb) double perovskites. All compositions have the monoclinic $P2_1/n$ superstructure with a fully ordered arrangement of Li^+ and Ru^{5+} cations. As the Ln-size decreases, the lattice volume decreases due to the increased tilting of the octahedra, but the Li−O and Ru−O distances remain constant. Antiferromagnetic transitions with Néel temperatures in the 20−35 K range were observed for all compositions, except for Gd_2LiRuO_6, which does not order down to 5 K. Nd_2LiRuO_6 shows a field-induced ferrimagnetic transition at ∼4 Tesla. The Ln = Pr, Nd, and Tb materials have type I magnetic structures with coupled spin ordering on the Ln and Ru sublattices. Critical fits reveal that the Ln^{3+} sublattice magnetization shows mean field behaviour ($\beta \approx 0.5$), whereas the Ru^{5+} spin order is consistent with the three-dimensional Heisenberg model ($\beta = 0.31-0.35$).

Introduction

Double perovskites have attracted much interest because of the large low-field magnetoresistances and spin-polarized conduction observed in Sr_2FeMoO_6 and other itinerant ferrimagnetic double perovskites.[1,2] Electrically insulating ferromagnetic double perovskites are rare but of potential interest for their magnetoelectric properties.[3] One notable insulating ferromagnet is Ca_2CrSbO_6, which has a Curie temperature of 16 K.[4,5] The ferromagnetism in this material results from the large octahedral tilting due to the size mismatch between the $(Cr/Sb)O_6$ framework and the small Ca^{2+} cations. The large tilting leads to a twisted arrangement of the Cr^{3+} t_{2g}^3 orbitals along the Cr−O−Sb−O−Cr bonds, which favours ferromagnetic, potential (correlation) superexchange over the usually dominant antiferromagnetic, kinetic (delocalization) superexchange for non-twisted bonds.[5] Indeed Sr_2CrSbO_6, which has a much reduced octahedral tilting due to the larger size of the Sr^{2+} cations, is antiferromagnetic ($T_N = 12$ K).[5] The aim of this work was to induce ferromagnetism in the Ln_2LiRuO_6 double perovskites with half-filled Ru^{5+} t_{2g}^3 orbitals by decreasing the lanthanide size. In addition, ruthenates have attracted much interest due to their unusual magnetic and electronic properties such as non-s-wave superconductivity in Sr_2RuO_4,[6] non-Fermi-liquid behaviour in $La_4Ru_6O_{19}$,[7] and orbital ordering in $La_4Ru_2O_{10}$.[8] The perovskite $SrRuO_3$ is a rare example of a 4d ferromagnet ($T_c \approx 165$ K).[9]

Double perovskites A_2MRuO_6 are characterized by a rock salt ordered arrangement of the M and Ru cations. M/Ru cation ordering does not necessarily occur and the cations may also be statistically disordered ($AM_{1/2}Ru_{1/2}O_3$). Two large classes of ruthenate double perovskites can be distinguished: (a) M = 3d metal and (b) M = lanthanide (including Y, La), where the A cations are chosen from Ca, Sr, Ba, La, or one of the lanthanides. The extent of rock salt cation ordering is primarily determined by the charge and size differences between the M and Ru cations.[10]

The early 3d metals (Cr−Fe) tend to have a +3 oxidation state in ruthenium oxides and form disordered perovskites,[11−15] whereas the later ones (Co−Zn) can be stabilized as +2 by using appropriate A-site cations[12,16−23] and form the ordered

* Corresponding author. E-mail: j.w.g.bos@ed.ac.uk.
† University of Edinburgh.
‡ Ludwig-Maximilians-University.
§ Institut Laue-Langevin.

(1) Kobayashi, K. L.; Kimura, T.; Sawada, H.; Terakura, K.; Tokura, Y. *Nature* **1998**, *395*, 677–680.
(2) Serrate, D.; De Teresa, J. M.; Ibarra, M. R. *J. Phys.: Condensed Matter* **2007**, *19*, 023201.
(3) Azuma, M.; Takata, K.; Saito, T.; Ishiwata, S.; Shimakawa, Y.; Takano, M. *J. Am. Chem. Soc.* **2005**, *127*, 8889.
(4) Retuerto, M.; Alonso, J. A.; Garcia-Hernandez, M.; Martinez-Lope, M. J. *Solid State Commun.* **2006**, *139*, 19.
(5) Retuerto, M.; Garcia-Hernandez, M.; Martinez-Lopez, M. J.; Fernandez-Diaz, M. T.; Attfield, J. P.; Alonso, J. A. *J. Mater. Chem.* **2007**, *17*, 3555.
(6) Maeno, Y.; Hashimoto, H.; Yoshida, K.; Nishizaki, S.; Fujita, T.; Bednorz, J. G.; Lichtenberg, F. *Nature* **1994**, *372*, 532.
(7) Khalifah, P.; Nelson, K. D.; Jin, R.; Mao, Z. Q.; Liu, Y.; Huang, Q.; Gao, X. P. A.; Ramirez, A. P.; Cava, R. J. *Nature* **2001**, *411*, 669.
(8) Khalifah, P.; Osborn, R.; Huang, Q.; Zandbergen, H. W.; Jin, R.; Liu, Y.; Mandrus, D.; Cava, R. J. *Science* **2002**, *297*, 2237.
(9) Klein, L.; Dodge, J. S.; Ahn, C. H.; Reiner, J. W.; Mieville, L.; Geballe, T. H.; Beasley, M. R.; Kapitulnik, A. *J. Phys.: Condensed Matter* **1996**, *8*, 10111.
(10) Anderson, M. T.; Greenwood, K. B.; Taylor, G. A.; Poeppelmeier, K. R. *Prog. Solid State Chem.* **1993**, *22*, 197.
(11) Bune, R. O.; Lobanov, M. V.; Popov, G.; Greenblatt, M.; Botez, C. E.; Stephens, P. W.; Croft, M.; Hadermann, J.; Van Tendeloo, G. *Chem. Mater.* **2006**, *18*, 2611.
(12) Dass, R. I.; Yan, J. Q.; Goodenough, J. B. *Phys. Rev. B* **2004**, *69*, 094416.

10.1021/cm8020935 CCC: $40.75
Published on Web 12/23/2008

double perovskite superstructure. Examples of double perovskites are $(AA')CoRuO_6$ (A = La; A′ = Ca, Sr, Ba or La),[18−20,22] whereas Sr_2CoRuO_6[22] and $(AA')MnRuO_6$ are B-site disordered.[11−13] The disordered ruthenate perovskites (Cr−Fe) are ferromagnetic or show glassy magnetic behaviour, whereas the ordered compositions (Co−Zn) are mostly antiferromagnetic. Both ordered and disordered 3d ruthenates are semiconductors, with the disordered materials typically having larger conductivities.

The lanthanide A_2LnRuO_6 double perovskites have an ordered double perovskite structure for A = Ca, Sr, and Ba.[24−36] The small size of Ca can result in a mixing of the A- and B-site cations.[36] These materials are generally antiferromagnetic insulators, but the low-temperature magnetic susceptibilities of some compositions (e.g., Sr_2TbRuO_6)[28] show a ferromagnetic component. Neutron powder diffraction studies reveal antiferromagnetic ordering of both the Ru^{5+} and Ln^{3+} sublattices.[24−27,29,30,36]

Ruthenium double perovskites also form with the alkali earth metals (M = Li, Na) with a lanthanide ion on the A-site. The structural and magnetic properties of the Ln_2NaRuO_6 materials (Ln = La, Pr, Nd) have been reported by Gemmill et al.[37] All three oxides crystallize with the monoclinic $P2_1/n$ superstructure. Magnetic measurement show that La_2NaRuO_6 is antiferromagnetic (T_N = 16 K), whereas the Pr and Nd materials have a ferromagnetic component ($T_c \approx 20$ K) in their magnetic susceptibilities. No neutron diffraction studies have been reported. La_2LiRuO_6 was studied by Battle et al. and has the $P2_1/n$ double perovskite superstructure.[38] Neutron powder diffraction revealed antiferromagnetic ordering below the Néel temperature of 30 K with an ordered moment of 2.2(2) μ_B/Ru. We report upon the synthesis, structures and magnetic properties of the Ln_2LiRuO_6 double perovskites with Ln = Pr, Nd, Sm, Eu, Gd, and Tb. To the best of our knowledge, this is the first report of a neutron powder diffraction study of a (ruthenium) double perovskite system with both A- and B-site magnetic order.

Experimental Section

The compounds Ln_2LiRuO_6 (Ln = La, Pr, Nd, Sm, Eu, Gd, Tb) were synthesized as polycrystalline samples by standard solid-state chemistry techniques. Stoichiometric quantities of Ln_2O_3 (dried at 1000 °C for 12 h) and RuO_2 (dried at 450 °C for 12 h) and a 20 mol % excess of Li_2CO_3 (dried at 80 °C for 12 h) were ground together and pressed into a pellet, which was sintered at 980 °C for 12 h. The pellet was reground, an additional 20 mol% excess of Li_2CO_3 was added and intimately ground with the sample. After pressing the powder into a pellet a final sintering was performed at 980 °C for 12 h. The addition of Li_2CO_3 in excess is needed because of the volatilization of Li and is essential for the synthesis of phase-pure samples. For the neutron powder diffraction measurements of Ln = Pr, Nd, and Tb, 5 g samples were synthesized following the same procedure. The phase purity of the samples was confirmed by laboratory X-ray powder diffraction on a Bruker D8 Advance diffractometer with monochromated $CuK_{\alpha 1}$ radiation. Patterns to be used for Rietveld refinement were collected in Bragg Brentano geometry with a step size of 0.007° over the angular range $5° \le 2\theta \le 100°$. No reflections attributable to Li containing impurity phases were found in any of the patterns. For the smaller lanthanides minor Ln_2O_3 impurities were present. Room temperature synchrotron X-ray diffraction data were collected on the BM01 (Ln = Gd) and ID31 (Ln = Sm, Eu) instruments at the European Synchrotron Radiation Facility in Grenoble, France. For BM01, λ = 0.5001 Å and data were collected between $5° \le 2\theta \le 30°$ with a 0.003° stepsize. For ID31: λ = 0.3983 Å and data were collected between $1° \le 2\theta \le 35°$ with a 0.001° stepsize. Neutron powder diffraction patterns were collected on the D2B and D1B instruments at the Institute Laue Langevin in Grenoble, France. The wavelength for D2B was 1.594 Å and data were collected between $5° \le 2\theta \le 160°$ with a 0.05° stepsize. The D1B data were collected with λ = 2.52 Å in the $5° \le 2\theta \le 100°$ interval with a 0.2° stepsize. The D2B data were used to determine the detailed crystal and magnetic structures while the temperature evolution of the magnetic scattering was followed using the D1B instrument. The GSAS suite of programs was used for the Rietveld fitting of the laboratory X-ray, synchrotron X-ray and neutron diffraction data.[39,40] A Debye-Scherrer absorption correction was used in the refinement of the powder diffraction data. This had no effect on the refined atomic coordinates. The magnetic susceptibilities of the samples were measured between 5−350 K in H = 250 Oe using a Quantum Design Magnetic Property Measurement System 2.0 SQUID magnetometer. The zero-field-cooled and field-cooled measurements were found to overlie. In addition M(H) measurements were performed using the ACMS insert of a Quantum Design Physical Property Measurement System.

(13) Horikubi, T.; Kamegashira, N. *Mater. Chem. Phys.* **2000**, *65*, 316.
(14) Mamchik, A.; Chen, I. W. *Phys. Rev. B* **2004**, *70*, 104409.
(15) Williams, A. J.; Gillies, A.; Attfield, J. P.; Heymann, G.; Huppertz, H.; Martinez-Lope, M. J.; Alonso, J. A. *Phys. Rev. B* **2006**, *73*, 104409.
(16) Attfield, M. P.; Battle, P. D.; Bollen, S. K.; Kim, S. H.; Powell, A. V.; Workman, M. *J. Solid State Chem.* **1992**, *96*, 344.
(17) Battle, P. D.; Gibb, T. C.; Jones, C. W.; Studer, F. *J. Solid State Chem.* **1989**, *78*, 281.
(18) Bos, J. W. G.; Attfield, J. P. *Chem. Mater.* **2004**, *16*, 1822.
(19) Bos, J. W. G.; Attfield, J. P. *Phys. Rev. B* **2004**, *69*, 094434.
(20) Bos, J. W. G.; Attfield, J. P. *J. Mater. Chem.* **2005**, *15*, 715.
(21) Gateshki, M.; Igartua, J. M. *Mater. Res. Bull.* **2003**, *38*, 1893.
(22) Kim, S. H.; Battle, P. D. *J. Solid State Chem.* **1995**, *114*, 174.
(23) Hong, K. P.; Choi, Y. H.; Kwon, Y. U.; Jung, D. Y.; Lee, J. S.; Shim, H. S.; Lee, C. H. *J. Solid State Chem.* **2000**, *150*, 383.
(24) Battle, P. D.; Jones, C. W. *J. Solid State Chem.* **1989**, *78*, 108.
(25) Battle, P. D.; Jones, C. W.; Studer, F. *J. Solid State Chem.* **1991**, *90*, 302.
(26) Battle, P. D.; Macklin, W. J. *J. Solid State Chem.* **1984**, *52*, 138.
(27) Battle, P. D.; Macklin, W. J. *J. Solid State Chem.* **1984**, *54*, 245.
(28) Doi, Y.; Hinatsu, Y. *J. Phys.: Condensed Matter* **1999**, *11*, 4813.
(29) Doi, Y.; Hinatsu, Y.; Nakamura, A.; Ishii, Y.; Morii, Y. *J. Mater. Chem.* **2003**, *13*, 1758.
(30) Doi, Y.; Hinatsu, Y.; Oikawa, K.; Shimojo, Y.; Morii, Y. *J. Alloys Compd.* **2001**, *323*, 455.
(31) Hinatsu, Y.; Doi, Y. *Bull. Chem. Soc. Jpn.* **2003**, *76*, 1093.
(32) Hinatsu, Y.; Izumiyama, Y.; Doi, Y.; Alemi, A.; Wakeshima, M.; Nakamura, A.; Morii, Y. *J. Solid State Chem.* **2004**, *177*, 38.
(33) Izumiyama, Y.; Doi, Y.; Wakeshima, M.; Hinatsu, Y.; Nakamura, A.; Ishii, Y. *J. Solid State Chem.* **2002**, *169*, 125.
(34) Izumiyama, Y.; Doi, Y.; Wakeshima, M.; Hinatsu, Y.; Oikawa, K.; Shimojo, Y.; Morii, Y. *J. Mater. Chem.* **2000**, *10*, 2364.
(35) Izumiyama, Y.; Doi, Y.; Wakeshima, M.; Hinatsu, Y.; Shimojo, Y.; Morii, Y. *J. Phys.: Condensed Matter* **2001**, *13*, 1303.
(36) Sakai, C.; Doi, Y.; Hinatsu, Y.; Ohoyama, K. *J. Phys.: Condensed Matter* **2005**, *17*, 7383.
(37) Gemmill, W. R.; Smith, M. D.; zur Loye, H. C. *J. Solid State Chem.* **2004**, *177*, 3560.
(38) Battle, P. D.; Grey, C. P.; Hervieu, M.; Martin, C.; Moore, C. A.; Paik, Y. *J. Solid State Chem.* **2003**, *175*, 20.
(39) Larson, A. C.; Von Dreele, R. B. *General Structure Analysis System (GSAS)*, Los Alamos National Laboratory Report LAUR 86-748; Los Alamos National Laboratory: Los Alamos, NM, 2000.
(40) Toby, B. H. *J. Appl. Crystallogr.* **2001**, *34*, 210.

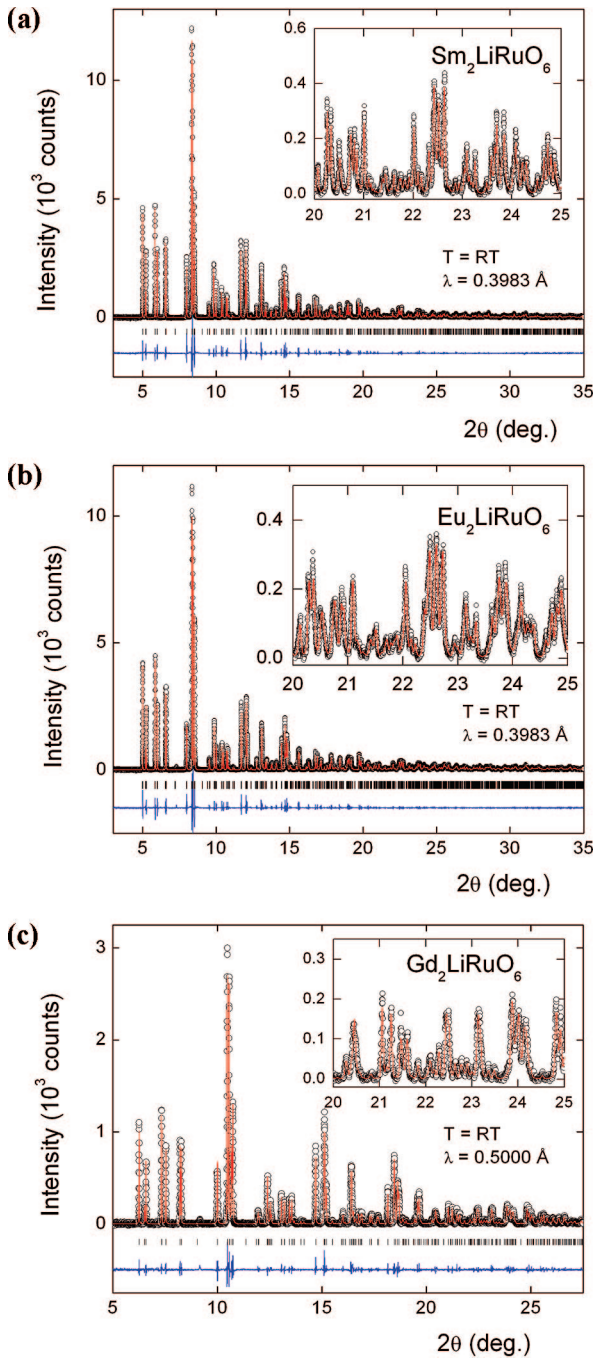

Figure 1. Observed (o), calculated (–), and difference room temperature (RT) synchrotron powder diffraction Rietveld profiles for (a) Sm_2LiRuO_6, (b) Eu_2LiRuO_6, and (c) Gd_2LiRuO_6. The markers indicate the position of the structural Bragg reflections. Small traces of Ln_2O_3 impurities are visible in (b) at 7.3° and in (c) at 9.2°.

Results

Crystal Structure. Rietveld analysis of the laboratory, synchrotron X-ray, and neutron diffraction data revealed that all Ln_2LiRuO_6 double perovskites crystallize with the monoclinic $P2_1/n$ superstructure. This is in agreement with the earlier work on La_2LiRuO_6. The fits to the room temperature (RT) synchrotron diffraction data are shown in Figure 1. The structural analysis also confirms the fully ordered rock salt arrangement of the Li^+ and Ru^{5+} cations in all samples. The lattice constants (a, b, $c/\sqrt{2}$) converge towards a value between 5.5−5.6 Å with increasing A-site (Ln^{3+}) ionic radius

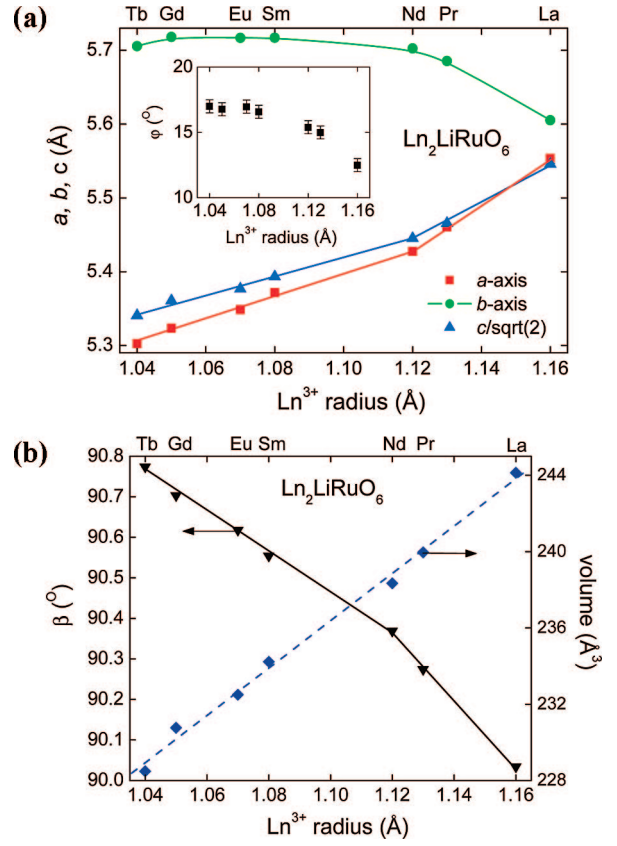

Figure 2. Lanthanide ionic radius dependence of the lattice constants for the Ln_2LiRuO_6 series. The inset shows the Ln^{3+} radius dependence of the average octahedral tilt angle φ.

(Fig. 2). The unit cell volume shows a linear dependence on the A-site radius. The monoclinic angle and a, c axes show two linear regions with the crossover occurring at the Nd composition. The b-axis has a very different temperature dependence; it initially increases rapidly (La−Nd), followed by a broad maximum (Sm−Gd), and then decreases slightly for Tb. The atomic parameters and selected bond lengths obtained from the Rietveld fitting of the neutron and synchrotron powder diffraction data are given in Table 1 and 2. The average Li−O and Ru−O bond lengths are within 3 standard deviations for the Ln_2LiRuO_6 series. All O−Li/Ru-O bond angles are within 2−3° of 90°. Bond valence sum (BVS) calculations confirm the Ru^{5+} and Li^+ oxidation states (Table 2).[41,42] The bond valence parameters for Ru^{5+} were taken from ref 19 The BVS for Ln^{3+} are somewhat lower than expected (~2.7) but are in excellent agreement with the value for La_2LiRuO_6 (BVS = 2.7).[38] Refinement of the atomic occupancies did not reveal any deviation from unity. The presence of four long Li−O and two short Li−O bonds is a general feature of Li double perovskite oxides and was already noted in ref 38. The RuO_6 octahedron is regular, as expected for the non-degenerate Ru^{5+} (t_{2g}^3) electronic configuration. The average Ln−O bond length is found to decrease in agreement with the decreasing ionic radii for the heavier lanthanides (Table 2). The average octahedral tilt angle can be estimated as $\varphi = (180 - \theta)/2$, where $\theta = \langle$Li−O−Ru$\rangle$ is the average Li−O−Ru bond

(41) Brese, N. E.; Okeeffe, M. *Acta Crystallogr., Sect. B* **1991**, *47*, 192.
(42) Brown, I. D.; Altermatt, D. *Acta Crystallogr., Sect. B* **1985**, *41* (AUG), 244.

Table 1. Overview of Refined Lattice Constants, Atomic Parameters, and Fit Statistics for the Ln_2LiRuO_6 Double Perovskites[a]

		Pr	Nd	Sm	Eu	Gd	Tb
a-axis (Å)		5.4580(1)	5.4206(1)	5.37395(2)	5.35163(3)	5.2336(1)	5.30826(3)
b-axis (Å)		5.6855(1)	5.7023(1)	5.72164(3)	5.71895(3)	5.7181(1)	5.68438(3)
c-axis (Å)		7.7258(2)	7.6914(2)	7.63042(3)	7.60795(4)	7.5811(1)	7.53588(4)
β (deg)		90.285(1)	90.391(2)	90.561(1)	90.615(1)	90.704(1)	90.706(1)
V (Å^3)		239.74(1)	237.74(1)	234.607(2)	232.833(3)	230.76(1)	227.37(3)
Ln	*x*	0.0131(7)	0.0130(5)	0.01606(9)	0.01697(8)	0.0177(2)	0.0154(9)
	y	0.9406(5)	0.9359(4)	0.92946(6)	0.92715(5)	0.9251(1)	0.9232(7)
	z	0.7883(5)	0.7492(4)	0.74898(8)	0.74891(6)	0.7485(1)	0.7489(6)
	U_{iso}	0.0121(7)	0.0060(7)	0.0057(1)	0.0052(1)	0.0015(3)	0.007(1)
Li	U_{iso}	0.0092(7)	0.007(1)	0.0014(2)	0.0012(2)	0.0031(6)	0.010(2)
Ru	U_{iso}	0.0092(7)	0.007(1)	0.0014(2)	0.0012(2)	0.0031(6)	0.010(21)
O1	*x*	0.2904(5)	0.2921(7)	0.2964(8)	0.2991(7)	0.303(2)	0.309(1)
	y	0.6896(5)	0.6883(7)	0.6902(9)	0.6858(8)	0.684(2)	0.684(1)
	z	0.9561(4)	0.9549(5)	0.9518(6)	0.9503(5)	0.951(1)	0.9500(9)
	U_{iso}	0.0115(4)	0.0102(6)	0.0030(7)	0.0025(6)	0.00(2)	0.0105(9)
O2	*x*	0.1850(5)	0.1844(7)	0.1757(8)	0.1764(7)	0.181(2)	0.174(1)
	y	0.2128(5)	0.2122(7)	0.2081(9)	0.2079(8)	0.206(2)	0.201(1)
	z	0.9522(3)	0.9501(4)	0.9484(6)	0.9467(5)	0.948(1)	0.9436(9)
	U_{iso}	0.0115(4)	0.00102(6)	0.0030(7)	0.0025(6)	0.00(2)	0.0105(9)
O3	*x*	0.9116(5)	0.9087(6)	0.8990(8)	0.8974(7)	0.902(2)	0.890(1)
	y	0.5251(5)	0.5262(6)	0.5345(8)	0.5340(7)	0.536(2)	0.538(1)
	z	0.7566(4)	0.7551(5)	0.7578(6)	0.7549(5)	0.754(1)	0.7565(8)
	U_{iso}	0.0115(4)	0.00102(6)	0.0030(7)	0.0025(6)	0.00(2)	0.0105(9)
χ^2		1.7	1.7	3.7	2.9	1.3	1.0
wR_p (%)		8.0	7.5	13.8	12.5	15.1	10.7
R_p (%)		6.4	5.9	11.2	10.1	11.3	8.4
temperature		RT	RT	RT	RT	RT	4 K
instrument		D2B	D2B	ID31	ID31	BM01	D2B

[a] SG = $P12_1/n1$; Ln, O1, O2, and O3 on 4*e* (*x*,*y*,*z*); Li on 2*b* (1/2, 0, 0) and Ru on 2*d* (1/2, 0, 1/2). U_{iso} units are Å^2.

Table 2. Selected Bond Lengths (Å), Angles (deg), and Bond Valence Sums for the Ln_2LiRuO_6 Double Perovskites

	Pr	Nd	Sm	Eu	Gd	Tb
Li−O1	2.129(3)	2.132(4)	2.113(5)	2.126(4)	2.13(1)	2.091(7)
Li−O2	2.133(3)	2.128(4)	2.144(5)	2.136(4)	2.107(9)	2.113(7)
Li−O3	2.047(3)	2.032(4)	2.055(5)	2.031(4)	2.019(9)	2.038(6)
⟨Li−O⟩	2.103(3)	2.097(4)	2.104(5)	2.098(4)	2.085(9)	2.081(7)
BVS	1.08	1.10	1.08	1.10	1.13	1.14
Ru−O1	1.948(3)	1.946(4)	1.967(5)	1.961(4)	1.968(9)	1.989(7)
Ru−O2	1.956(3)	1.961(4)	1.960(5)	1.963(4)	1.984(10)	1.982(7)
Ru−O3	1.945(3)	1.950(4)	1.931(5)	1.948(4)	1.945(9)	1.931(7)
⟨Ru−O⟩	1.950(3)	1.952(4)	1.953(5)	1.957(4)	1.966(9)	1.967(7)
BVS	5.11	5.07	5.07	5.00	4.89	4.88
⟨Ln−O⟩	2.522(4)	2.506(5)	2.476(5)	2.465(4)	2.463(9)	2.432(8)
BVS	2.75	2.61	2.70	2.69	2.64	2.68
Li−O1−Ru	150.2(2)	149.4(2)	148.3(3)	146.7(2)	146.0(5)	144.7(5)
Li−O2−Ru	149.0(2)	148.3(2)	145.9(3)	145.6(2)	146.3(5)	143.5(4)
Li−O3−Ru	150.8(2)	149.9(2)	146.3(2)	145.9(2)	147.0(5)	143.3(4)
⟨Li−O−Ru⟩	150.0(2)	149.2(2)	146.8(3)	146.1(2)	146.4(5)	143.8(4)

angle, given in Table 2. The RT values of φ are shown in the inset to Figure 2. The value for Ln = La (φ = 12.5°) was taken from ref 38, whereas the RT value for Ln = Tb (φ = 17.1°) was obtained from a Rietveld fit to laboratory X-ray data. The inset reveals that φ initially increases rapidly but that it flattens of for the smaller lanthanides. This suggests that the structure is not able to tolerate much larger tilt angles than $\varphi \approx 17°$. For Ln = Dy and Y, the perovskite structure is not stable and instead a different phase is observed. From LeBail fitting for Ln = Dy, this phase has cell constants *a* = 3.6432(1) Å, *b* = 5.8522(1) Å, and *c* = 11.7842(2) Å and is I-centered. Attempts to solve the crystal structure are underway and will not be further discussed in this manuscript.

Magnetization. The zero field cooled magnetic susceptibilities of the Ln_2LiRuO_6 series are shown in Figure 3. Antiferromagnetic transitions are apparent for Ln = La, Pr, Sm, Eu, and Tb (Néel temperatures are given in Table 3). The susceptibility for Ln = Gd deviates from Curie−Weiss paramagnetic below ~20 K but no magnetic transition is

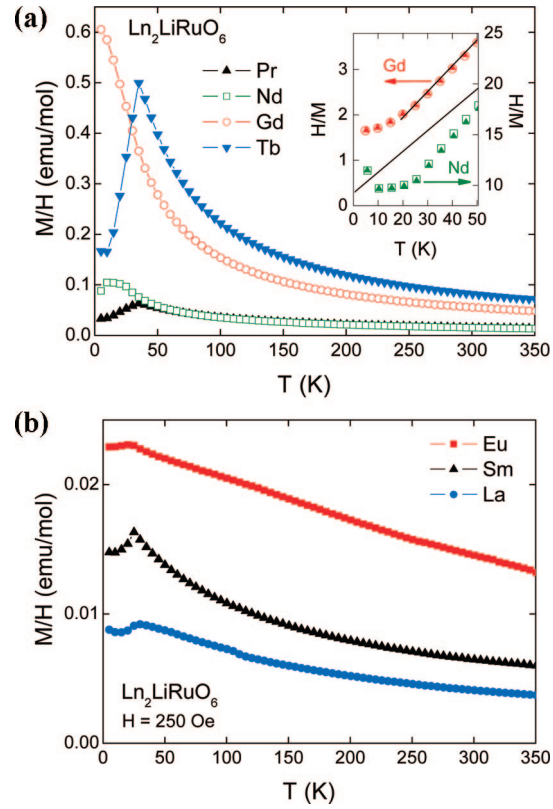

Figure 3. Temperature dependence of the magnetic susceptibilities for the Ln_2LiRuO_6 series. The inset shows the inverse magnetic susceptibilities for Ln = Nd and Gd. The solid lines are extrapolated Curie–Weiss fits. Note that Ln = Eu does not show Curie−Weiss behaviour, which is due to the low-lying first excited magnetic state.

observed down to 5 K (inset to Fig 3a). The inset also illustrates the low temperature inverse susceptibility for Ln = Nd, which is characterized by a plateau and does not show a sharp antiferromagnetic transition. The temperature de-

Table 3. Curie Constants (C), Effective Moments (μ_{exp}), and Weiss Temperatures (θ) Obtained from Curie−Weiss Fits to the High-Temperature (125−350 K) Magnetic Susceptibilities; Néel Temperatures and Expected (μ_{calcd}) Effective Moments Are Also Given

	La	Pr	Nd	Sm	Eu	Gd	Tb
C (emu K mol^{-1})	1.90	5.61	4.98	1.74		17.56	25.52
θ (K)	−167	−65	−47	−100		−15	−24
T_N (K)	30	31	19	25	20	<5	35
μ_{exp} (μ_B)	3.9	6.7	6.3	3.7		11.9	14.3
μ_{calcd} (μ_B)[a]	3.9	6.4	6.4	4.1		11.9	14.3

[a] $\mu_{calcd}^2 = 2\mu_{Ln}^2 + \mu_{Ru}^2$, where $\mu_{Ln} = g_J[J(J+1)]^{1/2}$ and $\mu_{Ru} = 2[S(S+1)]^{1/2}$ with $S = 3/2$. g_J is the Lande factor and J the quantum number for the total angular momentum.

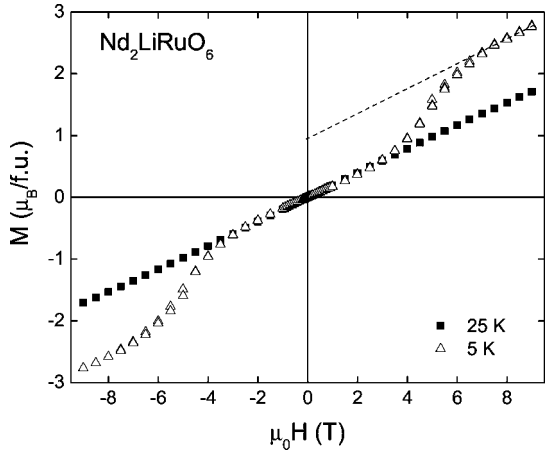

Figure 4. Field dependence of the magnetization at 5 and 25 K for Nd_2LiRuO_6.

pendences of the magnetic susceptibilities between 125−350 K are described satisfactorily using the Curie−Weiss law, except for Ln = Eu, where the low-lying first excited magnetic state modifies the temperature dependence. The fitted Curie constants and Weiss temperatures are listed in Table 3. The derived effective paramagnetic moments are in excellent agreement with those expected for a combination of $2Ln^{3+}$ and spin-only Ru^{5+} moments (Table 3). The Weiss temperatures are negative, indicating dominant antiferromagnetic interactions but do not show a regular dependence on A-site radius. Likewise, the Néel temperature does not vary in a systematic manner with A-site radius. The field dependence of the magnetization for Nd_2LiRuO_6 at 5 K reveals a metamagnetic transition at ∼4 Tesla (Figure 4). Extrapolation of the high-field magnetization reveals a magnetization of ∼ 0.8 μ_B per formula unit in the high-field state. The transition is absent in the 25 K magnetization isotherm (Figure 4). The other members of this series do not show this transition.

Magnetic Structure. The presence of long-range antiferromagnetic order in the Ln = Pr, Nd, and Tb samples was confirmed by the observation of magnetic Bragg reflections in the 4 K D2B diffraction patterns (Figure 5). These were all indexed by a magnetic cell doubled in the crystallographic a- and b-directions, so the magnetic propagation vector is $\mathbf{k}$ = (1/2 1/2 0). The absence of a doubling in the c-direction indicates that the magnetic order has dominant nearest neighbour antiferromagnetic exchange (type I). Magnetic symmetry analysis using the

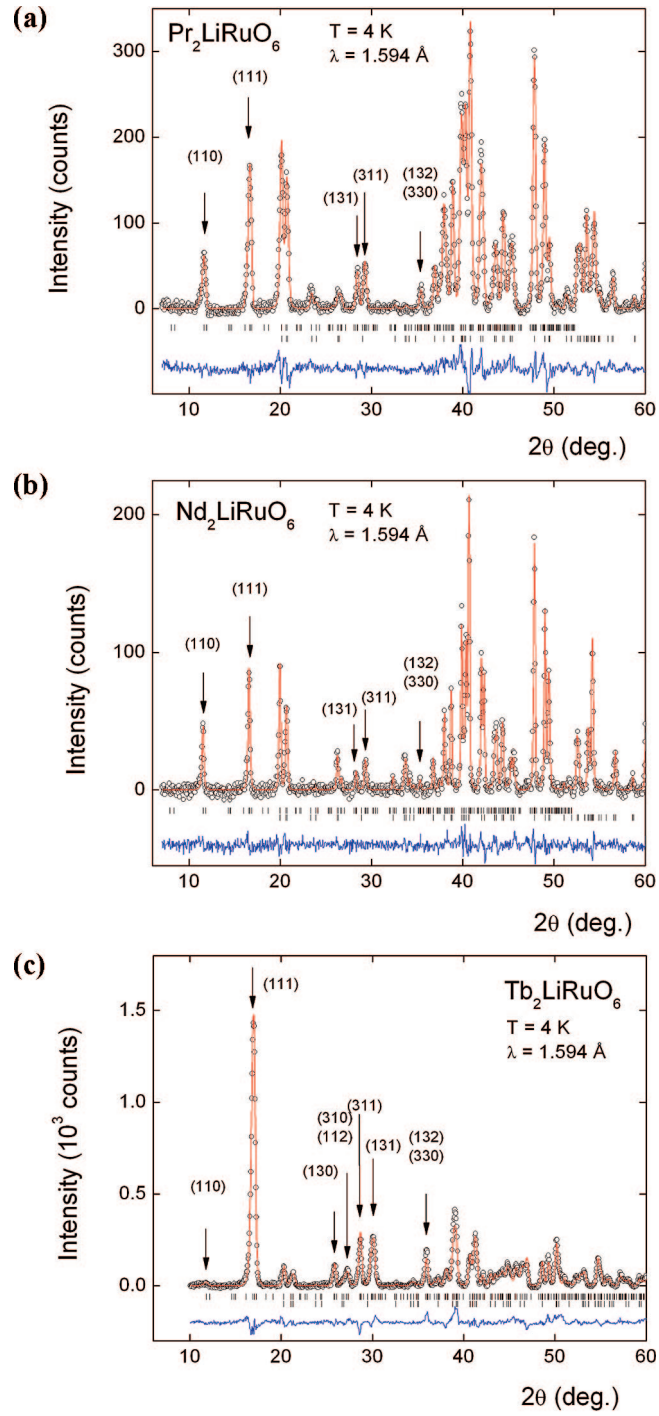

Figure 5. Observed (o), calculated (−), and difference 4 K neutron powder diffraction Rietveld profiles for (a) Pr_2LiRuO_6, (b) Nd_2LiRuO_6, and (c) Tb_2LiRuO_6. The upper (lower) markers indicate the position of the magnetic (structural) Bragg reflections. The arrows mark prominent magnetic reflections.

SARAh representation analysis program[43] was used to obtain possible models for the magnetic structure. We have employed this route previously for other double perovskites.[20,44] For the Ln_2LiRuO_6 materials, the small group (G_k) coincides with the $P2_1/n$ space group. The decomposition of the magnetic representation (in terms of the nonzero irreducible representations of G_k) of the Ru and Nd sites

(43) Wills, A. S. *Phys. B: Condensed Matter* **2000**, *276*, 680.
(44) Bos, J. W. G.; Attfield, J. P. *Phys. Rev. B* **2004**, *70*, 174434.

Table 4. Magnetic Models, Refined Ru and Ln Magnetic Moments, Angles between Moments, and Rietveld Fit Statistics at 4 K for Ln_2LiRuO_6 (Ln = Pr, Nd, Tb)[a]

		Pr		Nd		Tb	
		$3\Gamma_2$	$3\Gamma_4$	$3\Gamma_2$	$3\Gamma_4$	$3\Gamma_2$	$3\Gamma_4$
Ru1		$[v_1,v_2,v_3]$	$[v_1,v_2,v_3]$	$[v_1,v_2,v_3]$	$[v_1,v_2,v_3]$	$[v_1,v_2,v_3]$	$[v_1,v_2,v_3]$
Ru2		$[v_1,-v_2,v_3]$	$[-v_1,v_2,-v_3]$	$[v_1,-v_2,v_3]$	$[-v_1,v_2,-v_3]$	$[v_1,-v_2,v_3]$	$[-v_1,v_2,-v_3]$
Ln1		$[v_1,v_2,v_3]$	$[v_1,v_2,v_3]$	$[v_1,v_2,v_3]$	$[v_1,v_2,v_3]$	$[v_1,v_2,v_3]$	$[v_1,v_2,v_3]$
Ln2		$[-v_1,v_2,-v_3]$	$[v_1,-v_2,v_3]$	$[-v_1,v_2,-v_3]$	$[v_1,-v_2,v_3]$	$[-v_1,v_2,-v_3]$	$[v_1,-v_2,v_3]$
Ln3		$[-v_1,-v_2,-v_3]$	$[-v_1,-v_2,-v_3]$	$[-v_1,-v_2,-v_3]$	$[-v_1,-v_2,-v_3]$	$[-v_1,-v_2,-v_3]$	$[-v_1,-v_2,-v_3]$
Ln4		$[v_1,-v_2,v_3]$	$[-v_1,v_2,-v_3]$	$[v_1,-v_2,v_3]$	$[-v_1,v_2,-v_3]$	$[v_1,-v_2,v_3]$	$[-v_1,v_2,-v_3]$
Ru1	m_x	0.1(8)	0.1(7)	−0.1(6)	−0.2(6)	1.7(5)	−1.6(4)
	m_y	−0.1(6)	−0.1(6)	0.1(4)	−0.2(4)	0.4(3)	−0.5(3)
	m_z	−2.1(1)	−2.1(1)	−2.8(1)	−2.9(1)	1.2(2)	−1.1(2)
	m	2.1(1)	2.1(1)	2.8(1)	2.9(1)	2.1(4)	2.1(4)
Ln1	m_x	1.7(1)	1.7(1)	0.0(2)	0.0(2)	−6.6(1)	6.6(1)
	m_y	−1.6(1)	−1.6(1)	2.0(1)	−2.1(1)	5.9(1)	−5.9(1)
	m_z	−0.1(2)	−0.1(2)	−0.6(3)	−0.5(3)	0.9(3)	−0.9(2)
	m	2.3(1)	2.3(1)	2.1(1)	2.1(1)	8.9(1)	8.9(1)
∠Ru1−Ru2 (deg)		0	180	0	180	22	152
∠Ln1−Ln2 (deg)		94	86	34	153	96	83
∠Ln1−Ru1 (deg)		84	84	71	73	114	112
∠Ln1−Ru2 (deg)		87	93	75	99	132	45
∠Ln2−Ru1 (deg)		93	87	105	81	48	135
∠Ln2−Ru2 (deg)		96	96	109	107	66	68
χ^2		3.1	3.2	2.0	2.0	1.0	1.0
wR_p (%)		7.5	7.6	7.4	7.4	10.7	10.7
R_p (%)		6.4	6.7	6.2	6.2	8.4	8.4

[a] Ru and Ln positions: Ru1 (1/2 0 1/2); Ru2 (0 1/2 0); Ln1 (x, y, z); Ln2 (1/2 − x, y − 1/2, 1/2 − z); Ln3 (−x, −y, −z); Ln4 (1/2 + x, 1/2 − y, z − 1/2), where x, y, z correspond to the coordinates in Table 1. The estimated standard deviations on the angles between magnetic moments are approximately 10°.

is $\Gamma_{mag} = 3\Gamma_2^1 + 3\Gamma_4^1$ and $\Gamma_{mag} = 3\Gamma_1^1 + 3\Gamma_2^1 + 3\Gamma_3^1 + 3\Gamma_4^1$, respectively. The labeling follows the scheme used by Kovalev.[45] The associated basis vectors are given in Table 4 and reveal that the independent Ru and Ln sites can have their moments arranged in two possible ways, corresponding to $\Gamma_{mag} = 3\Gamma_2$ or $3\Gamma_4$. Initially, the symmetry allowed models were refined using the SARAh-Refine program, which utilizes a reverse Monte Carlo (RMC) algorithm to perform a global search sampling all regions of phase space with an equal probability.[43] Approximately 500 RMC cycles were run for the allowed magnetic models. Following these simulations, the best solutions were Rietveld (least squares) fitted to obtain the final solutions for the magnetic structures, which are given in Table 4. This revealed that the two models fit the data equally well and are therefore equivalent solutions. The $3\Gamma_1$ and $3\Gamma_3$ models with ordering of the Ln-sites only do not fit the magnetic intensities. The refined Ru moments for Ln = Pr (2.1(1) μ_B) and Tb (2.1(4) μ_B) are reduced compared to the expected spin-only value of 3 μ_B for Ru^{5+} (S = 3/2), whereas the fitted moment for Ln = Nd is in good agreement (2.8(1) μ_B). The expected moments for Pr^{3+} (3.2 μ_B) and Nd^{3+} (3.3 μ_B) are somewhat higher than the observed moments of 2.3(1) and 2.2(1) μ_B, respectively. The experimental Tb^{3+} moment (8.9(1) μ_B) is in very good agreement with the expected moment of 9 μ_B. The reduction of the observed magnetic moments may be indicative of magnetic frustration. Significant magnetic frustration has been previously observed in type I antiferromagnetic A_2LnRuO_6 double perovskites.[29,46] The refined magnetic structure of Nd_2LiRuO_6 ($3\Gamma_4$ solution) is shown in Figure 6a. The orientation of the Nd−Ru moments in the $3\Gamma_2$ and $3\Gamma_4$ solutions and the Nd−O−Ru connectivity are illustrated in Figure 6b. Variable temperature neutron powder diffraction data through the magnetic transition were collected for the Ln = Pr and Nd samples using the D1B instrument. The temperature dependence of the Rietveld fitted ordered magnetic moment of the Ru and Ln sublattices is shown in Figure 7. The Ru moments follow a normal critical behaviour in both samples with critical exponents β = 0.31 (Ln = Nd) and 0.35 (Ln = Pr), close to the expected value for a three-

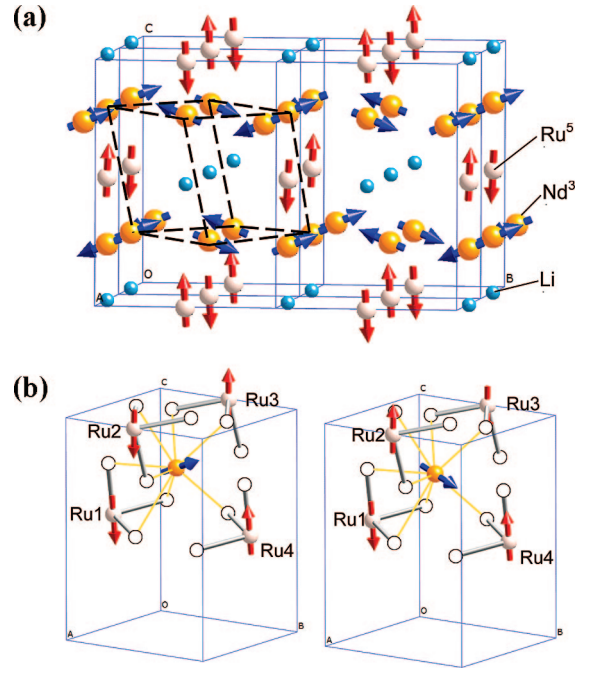

Figure 6. (a) Model of the final refined ($3\Gamma_4$) magnetic structure for Nd_2LiRuO_6 at 4 K. Nd, yellow circles, blue vectors; Ru, white circles, red vectors; and Li, light blue circles. The dashed box illustrates the (structural) primitive Nd sublattice. (b) Illustration of the relative orientation of the Nd2 and Ru moments and coordination in the $3\Gamma_2$ (left) and $3\Gamma_4$ (right) solutions. Oxygen ions, open circles; yellow lines indicate Ru−O bonds; bonds longer than 3 Å are not shown.

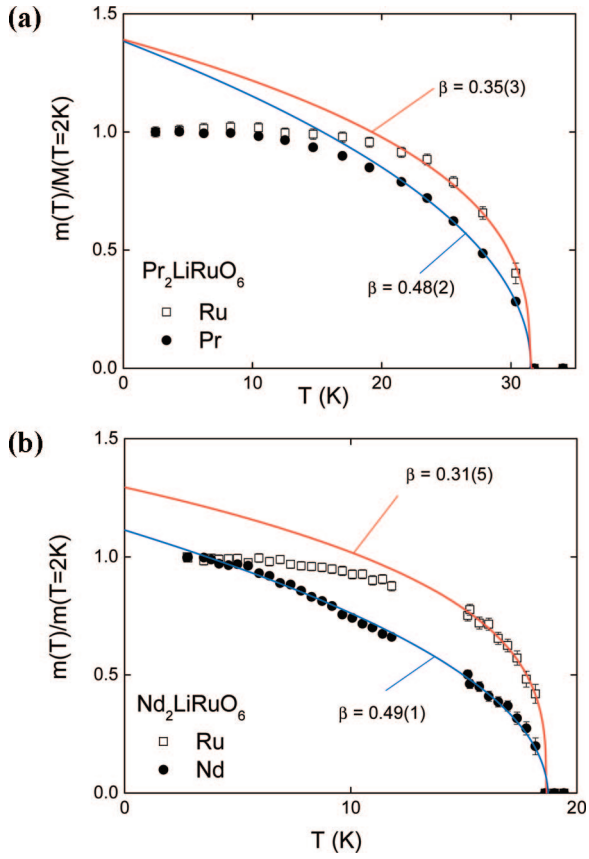

Figure 7. Temperature dependence of the ordered moment for the Pr (Nd) and Ru sublattices determined from Rietveld fits to D1B data. The solid lines are fits using a critical equation. The critical exponents are given in the figure.

dimensional Heisenberg magnet ($\beta = 0.367$). The Ln^{3+} moments in contrast have a flatter temperature dependence and a large critical exponent $\beta \approx 0.50$ is observed (Figure 7), which corresponds to the expected value from mean field theory. The fitted Néel temperatures are 31.5(3) and 18.7(2) K for Ln = Pr and Nd, respectively. (The data were fitted between 20 K $\leq T \leq T_N$ for Ln = Pr and 15 K $\leq T \leq T_N$ for Ln = Nd.)

Discussion

The detailed crystallographic study reveals that all Ln_2LiRuO_6 double perovskites crystallize with the monoclinic $P2_1/n$ superstructure with a gradual change in lattice constants and a fully ordered rock salt arrangement of Li and Ru. The Li/Ru−O bond distances do not depend on the A-site cation, and the dominant structural effect is an increase in the octahedral tilt angles with decreasing A-cation size. Two regions may be discerned here: for Ln = La−Nd, a substantial increase in the average tilt angle φ occurs, whereas for Ln = Sm−Tb, φ increases only modestly and is close to 17° (Figure 2). The lattice constants also reflect this crossover around Ln = Nd (Figure 2). The maximum average tilt angle observed in the isoelectronic Ln_2NaRuO_6 double perovskites is 19° (Ln = Nd). In contrast to the crystal structure, the magnetic properties do not vary in a systematic manner with A-site size. Gd_2LiRuO_6, does not order down to 5 K, while all other compositions show a Néel transition but no trend of T_N with any structural parameter is discernible. In addition, Nd_2LiRuO_6 shows a field-induced ferrimagnetic state, whereas the other lanthanides do not.

Most $A_2MM'O_6$ double perovskites have magnetic structures that are either type I or type II (Fig. 8).[26] This classification is based on the spin ordering of the M-cations and does not include the ordering of the A-site spins. In the following, type I and type II spin ordering will be briefly reviewed before discussing the combined A- and B-site spin order observed in the Ln_2LiRuO_6 double perovskites.

Type II Magnetic Order. Type II magnetic order is depicted in Figure 8a and is characterized by dominant next nearest neighbour (NNN) linear J_{180} M−O−M′−O−M antiferromagnetic (AF) exchange interactions. This leads to a doubling of the magnetic cell with respect to the ideal cubic double perovskite structure (space group $Fm\bar{3}m$; $a = 2a_p$, Figure 8a), and a magnetic propagation vector $\mathbf{k} = (1/2\ 1/2\ 1/2)$. In case of the common monoclinic $P2_1/n$ superstructure ($a = \sqrt{2}a_p$, $b = \sqrt{2}a_p$, $c = 2a_p$), the magnetic propagation vector is either $\mathbf{k} = (1/2\ 0\ 1/2)$ or $\mathbf{k} = (0\ 1/2\ 1/2)$.[44] Type II ordering is common in double perovskites where the B-site cations are both transition metals, such as La_2CoRuO_6.[20] We have previously shown that magnetic frustration effects are important in type II double perovskites.[44] Each M-cation occupies a face centred lattice, which consists of four primitive lattices in which the dominant NNN J_{180} M−O−M′−O−M AF exchange interactions are completely satisfied (Figure 8a). Frustration arises because the nearest neighbour (NN) J_{90} M−O−M′−O−M AF interactions connecting the four primitive lattices are frustrated: three paths are satisfied (dashed green lines in Figure 8a) and three are not (solid red lines). This effect is largest in cubic double perovskites (where the 12 J_{90} interactions are equivalent, note that each corner is connected by 2 J_{90}'s) and decreases with increasing octahedral tilting (the J_{90} interactions become inequivalent upon lowering symmetry, thereby reducing frustration), explaining the observed experimental trend of decreasing T_N with increasing A-site radius.[44]

Type I Magnetic Order. Type I magnetic order is characterized by dominant NN J_{90} M−O−M′−O−M AF exchange, leading to identical magnetic and nuclear cells. This is depicted in Figure 8b for the cubic double perovskite structure [$\mathbf{k} = 0$]. For monoclinic $P2_1/n$ double perovskites, the corresponding magnetic propagation vector $\mathbf{k} = (1/2\ 1/2\ 0)$. Type I ordering is common for double perovskites with a combination of a 4/5d metal and a lanthanide, e.g., Sr_2ErRuO_6.[25] In contrast with the type II structures discussed above, the experimental magnetic structures show that four paths are satisfied and two are not (dashed green and solid red lines in Figure 8b, respectively). This suggests that the frustration observed in type II materials might not be significant here. Indeed, experimentally, the Néel temperature is found to increase with increasing A-site radius (Table 2 in ref 36). This suggests that the dominant effect is the increase in M−O−M′−O−M orbital overlap resulting from the reduced octahedral tilting for larger A-site cations. This effect usually dominates in ABO_3 perovskites where the B-cations occupy a primitive cubic lattice, instead of the inherently frustrated face-centered lattice.

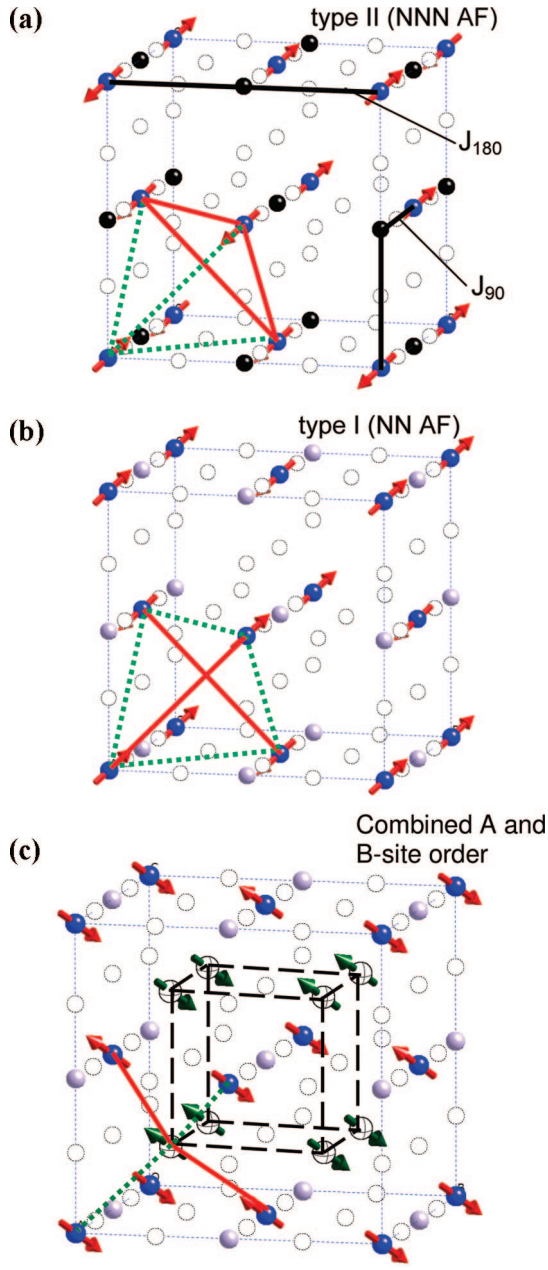

Figure 8. Type I and type II magnetic structures for $A_2MM'O_6$ double perovskites. The models shown are consistent with experimental solutions but have been transposed onto the ideal cubic double perovskite structure. (a) Type II magnetic ordering of the M-cations. The dominant J_{180} M−O−M′−O−M AF exchange interactions are completely satisfied in the four primitive M sublattices that make up the face centred M lattice. The relative orientation of the four primitive sublattices is determined by the weaker J_{90} M−O−M′−O−M AF exchange interactions. This can conveniently be represented as a tetrahedron of interactions where the experimental solutions reveal that 3 out of 6 (the dashed green lines) are satisfied, whereas the other 3 are not satisfied (solid red lines). This leads to frustration effects (see text). Note that there are a total of 12 J_{90} pathways connecting the corners of the M tetrahedron. (b) Type I magnetic ordering of the M-cations. Here, the J_{90} M−O−M′−O−M AF interactions are dominant (the J_{180} AF interactions are not considered). The experimental structures reveal that 4 out of 6 interactions connecting the corners of the M tetrahedron are satisfied. (c) Combined A and M magnetic ordering, based on the present work. The M sublattice ordering is of type I (as in b). The A-site ions occupy a primitive cubic lattice (indicated by the dashed cube), and the ordering is simplified to collinear antiferromagnetic. The A-cations are tetrahedrally surrounded by M cations, and the relative orientation of the moments is frustrated as indicated by the dashed green and solid red lines. [Black (blue) circles correspond to the M (M′) face-centered cubic lattice. Equatorial spheres correspond to the A-site primitive cubic lattice. Hollow spheres, oxygen ions.]

Ln_2LiRuO_6. The Ru−O−(Li)−O−Ru t_{2g} superexchange is expected to be stronger than the Ln−O−Ln and Ln−O−Ru 4f superexchange and determines the magnetic ordering temperature. This is supported by the similar Néel temperatures for La_2LiRuO_6 and the other members of the series. The neutron powder diffraction study of the Ln = Pr, Nd, and Tb materials revealed a magnetic propagation vector **k** = (1/2 1/2 0) and therefore type I magnetic ordering of the Ru spins. The key features of the experimental magnetic structures are summarized in Table 4 and Figure 6. There are two Ru sites in the magnetic unit cell, and the moments are coupled in two possible manners, corresponding to the $3\Gamma_2$ and $3\Gamma_4$ solutions. For the Ln = Pr and Nd materials only a sizable *z*-component remains, and the Ru1 and Ru2 moments are parallel ($3\Gamma_2$) or antiparallel ($3\Gamma_4$). Tb_2LiRuO_6 behaves differently and significant m_x and m_z components are found, resulting in angles of 22 and 152° between the Ru moments for the $3\Gamma_2$ and $3\Gamma_4$ solutions, respectively.

In contrast to the face-centered Ru sublattice, the Ln sublattice is primitive, as can be readily seen in Figure 8c. This figure shows the ideal cubic perovskite structure with type I ordering of the B-site spins and a collinear AF ordering of the A-site moments based on the current results. The A-site magnetic order is consistent with dominant J_{180} A−O−A AF exchange paths. The A-cations are tetrahedrally surrounded by four M cations (and four M′ cations), and the A-site ordering is frustrated with respect to the M-spin ordering (depicted by the dashed green and solid red lines in Fig. 8c). The ordering of the Ln sublattice in Ln_2LiRuO_6 is in fact more complicated than the collinear model presented in Fig. 8c. This occurs because the $3\Gamma_2$ and $3\Gamma_4$ solutions have four magnetic Nd sites, which correspond to two antiferromagnetic pairs: Ln1−Ln3 and Ln2−Ln4 (Table 4). The angle between Ln1 and Ln2 is close to 90° for the Pr and Tb materials but is more collinear for Ln = Nd (34° for $3\Gamma_2$ and 153° for $3\Gamma_4$), which is the composition that shows the field induced ferrimagnetic state. The cube of Nd-spins shown in Fig 6a further illustrates the difference with the collinear model in Figure 8c.

The final component of the discussion is the coupling between the Ln and Ru magnetic sublattices. The angles between the moments are given in Table 4. For Ln = Pr, the moments are within error orthogonal but they become more collinear for Ln = Nd and Tb. This suggests that the stronger monoclinic distortion for the smaller rare-earths relieves some of the inherent frustration in the orientation of the Ln and Ru moments (see Figure 8c). In general, the presence of perpendicular magnetic moments implies that the symmetric Heisenberg exchange ($\propto \mathbf{S}_1 \cdot \mathbf{S}_2$) is frustrated, and that the orientation of the moments ($\mathbf{S}_1$, $\mathbf{S}_2$) is instead determined by the weaker antisymmetric Dzyaloshinsky-Moriya exchange ($\propto \mathbf{S}_1 \times \mathbf{S}_2$). The convex temperature dependence of both the ordered Ln and Ru moments (Figure 7) reveals that the ordering of the A- and B-sublattices is coupled and not induced. An induced moment is character-

(45) Kovalev, O. V., *Representations of the Crystallographic Space Groups*, 2nd ed.; Gordon and Breach Science Publishers: Switzerland, 1993.
(46) Kuz'min, E. V.; Ovchinnikov, S. G.; Singh, D. J. *Phys. Rev. B* **2003**, *68*, 024409.

ized by a gradual increase in the ordered moment, and no saturation at low temperatures.[47] The mean field critical exponent for the Pr and Nd sublattice magnetization suggests that these moments feel a uniform magnetic background and no competition between antiferromagnetic near neighbour and ferromagnetic further neighbour interactions. The origin of this behavior is unclear at present but may have to do with the weak and partially frustrated 4f Ln−O−Ln/Ru superexchange. In contrast to the Ln_2LiRuO_6 double perovskites, the layered $Nd_2BaLiRuO_7$ Ruddlesden-Popper phase has separate ordering transitions, the Ru sublattice orders below 32 K, whereas the Nd sublattice starts to order below ∼20 K and is fully long range ordered below $T \approx 8$ K.[48] Nd_2LiRuO_6 is the only member of the series that shows a transition to a high field ferrimagnetic state ($M \approx 0.8\ \mu_B$/f.u.). The most plausible high-field state would be based on an a ferrimagnetic alignment of the Nd and Ru sublattices, leading to a net magnetization of $2 \times 2.1 - 2.8 = 1.4\ \mu_B$/f.u. (This is based on Nd^{3+} and Ru^{5+} moments determined by powder neutron diffraction in zero applied field.) A neutron diffraction study in an applied magnetic field, preferably using a single crystal, is needed to resolve the nature of the high-field ferrimagnetic transition.

In summary, we have synthesized the Ln_2LiRuO_6 double perovskites and investigated their magnetic and structural properties using synchrotron X-ray and neutron powder diffraction, and magnetic susceptibility measurements. All materials crystallize with the monoclinic $P2_1/n$ double perovskite superstructure with a fully ordered arrangement of Li^+ and Ru^{5+}. As the Ln size decreases, the lattice volume decreases because of the increased tilting of the octahedra but the Li−O and Ru−O distances remain constant. The Ln = Gd composition does not show a magnetic ordering transition down to 5 K, whereas all other compositions are antiferromagnetic with Néel temperatures between 20−35 K. A field induced ferrimagnetic state is observed for Nd_2LiRuO_6 above 4 Tesla. The ordered magnetic structures are of type I (nearest neighbour antiferromagnet) with coupled magnetic ordering of the Ln^{3+} (perovskite A-site) and the Ru^{5+} (perovskite B-site) sublattices. The absence of a clear trend of T_N with any structural parameter, the observation of coupled magnetic Ln−Ru order, the absence of Néel order for Gd_2LiRuO_6 and the field induced ferrimagnetism for Nd_2LiRuO_6 all suggest that the Ln^{3+} magnetic moment may be important in determining the magnetic properties of the Ln_2LiRuO_6 double perovskites.

Acknowledgment. J.W.G.B. acknowledges the Royal Society of Edinburgh for a personal research fellowship and the EPSRC for provision of beam time at the ESRF and ILL. Dr. Serena Margadonna, Dr. Simon Kimber, and Mr. Wei-Tin Chen are thanked for their help with the data collection.

CM8020935

(47) McLaughlin, A. C.; Sher, F.; Kimber, S. A. J.; Attfield, J. P. *Phys. Rev. B* **2007**, *76*, 094514.
(48) Rodgers, J. A.; Battle, P. D.; Grey, C. P.; Sloan, J. *Chem. Mater.* **2005**, *17*, 4362.